applied sciences

MDPI

Article

Frequency-Separated Attention Network for Image Super-Resolution

Daokuan Qu [1,2], Liulian Li [3] and Rui Yao [3,*]

[1] School of Information and Control Engineering, China University of Mining and Technology, Xuzhou 221116, China; qudaokuan_cumt@163.com
[2] School of Energy and Materials Engineering, Shandong Polytechnic College, Jining 272067, China
[3] School of Computer Science and Technology, China University of Mining and Technology, Xuzhou 221116, China
* Correspondence: ruiyao@cumt.edu.cn

Abstract: The use of deep convolutional neural networks has significantly improved the performance of super-resolution. Employing deeper networks to enhance the non-linear mapping capability from low-resolution (LR) to high-resolution (HR) images has inadvertently weakened the information flow and disrupted long-term memory. Moreover, overly deep networks are challenging to train, thus failing to exhibit the expressive capability commensurate with their depth. High-frequency and low-frequency features in images play different roles in image super-resolution. Networks based on CNNs, which should focus more on high-frequency features, treat these two types of features equally. This results in redundant computations when processing low-frequency features and causes complex and detailed parts of the reconstructed images to appear as smooth as the background. To maintain long-term memory and focus more on the restoration of image details in networks with strong representational capabilities, we propose the Frequency-Separated Attention Network (FSANet), where dense connections ensure the full utilization of multi-level features. In the Feature Extraction Module (FEM), the use of the Res ASPP Module expands the network's receptive field without increasing its depth. To differentiate between high-frequency and low-frequency features within the network, we introduce the Feature-Separated Attention Block (FSAB). Furthermore, to enhance the quality of the restored images using heuristic features, we incorporate attention mechanisms into the Low-Frequency Attention Block (LFAB) and the High-Frequency Attention Block (HFAB) for processing low-frequency and high-frequency features, respectively. The proposed network outperforms the current state-of-the-art methods in tests on benchmark datasets.

Keywords: densely connected structure; frequency-separated; channel-wise and spatial attention; image super-resolution

Citation: Qu, D.; Li, L.; Yao, R. Frequency-Separated Attention Network for Image Super-Resolution. *Appl. Sci.* **2024**, *14*, 4238. https://doi.org/10.3390/app14104238

Academic Editor: Andrea Prati

Received: 28 March 2024
Revised: 9 May 2024
Accepted: 15 May 2024
Published: 16 May 2024

1. Introduction

Image super-resolution is an ill-posed problem that transforms a given coarse, low-resolution (LR) image into a high-resolution (HR) image with refined details. Traditional super-resolution methods include interpolation, sparse coding [1], and neighbor embedding [2]. However, these methods do not effectively map LR images to HR images.

Recently, convolutional neural networks (CNNs) have demonstrated superior expressive capabilities compared to traditional methods, achieving outstanding performance and efficiency in various high-level imaging tasks. SRCNN [3] first upscales an LR image to the size of an HR image using bicubic interpolation and then applies a convolutional neural network to replace the traditional manual mapping from LR to HR images, surpassing most traditional methods. CSCN [4] and SCN [5] enhance network expressiveness by integrating the traditional super-resolution (SR) method and a sparse prior with key components of neural convolutional networks. The deeper the network, the stronger its non-linear mapping capability; however, this depth can also result in weakened information flow

and training difficulties. VDSR [6] focuses on residual learning of the differences between HR and LR images, further increasing the network depth. Additionally, the introduction of recursive modules [7,8] and memory modules [7] also enhances depth. FSRCNN [9] increases network depth by reducing the size of filters. FSRCNN [9] and ESPCN [10] introduced deconvolution and sub-pixel convolution layers, respectively, a structure later adopted by most networks. Tai et al. [11] and Lim et al. [12] further increased network depth using residual blocks, while Tong et al. [13] and Zhang et al. [14,15] introduced data particle geometrical divide algorithms to the field of super-resolution. The authors of [16] added numerous skip connections to mitigate information flow attenuation in overly deep networks. To enhance the network's ability to process high-frequency information, Zhao et al. [17] employed deep convolutional networks and ResNet for high-frequency information in images, while Zhou et al. [18] identified high-frequency features and increased their learning rates to improve the recovery of complex details in images.

Due to the optimal loss function for super-resolution problems being L_1, resulting in minimal loss values, the combination of small loss values and excessive layers in deep networks can lead to gradient vanishing. Consequently, it becomes challenging to effectively translate the potential expressive capabilities gained from increased network depth into the model's ability to learn the non-linear mapping from LR to HR images. Images contain high-frequency information representing texture details and low-frequency information describing object edges; similarly, features extracted by the network from LR images also consist of low- and high-frequency features. The use of numerous skip connections for dense connectivity allows for the full, adaptive integration of features across layers, and the use of memory modules achieves persistent memory, mitigating the effects of information flow attenuation caused by network depth. High-frequency features require more complex processing for detailed restoration compared to low-frequency features. However, the absence of an effective network structure to distinguish between high- and low-frequency information in images results in outputs where parts with complex textures appear smooth. Zhao et al. [17] and Zhou et al. [18] processed high- and low-frequency features separately, but in deep convolutional networks, some informative features may be overlooked.

To address these issues, we propose a Frequency-Separated Attention Network, termed FSANet, for image super-resolution. FSANet employs dense connections to fully integrate multi-level features for sustained memory, separately processes high- and low-frequency features to meet the demands of high-frequency feature processing, and utilizes channel and spatial attention to leverage informative features in both high- and low-frequency domains. In FSANet, we design an FEM for feature extraction and a Non-Linear Mapping Module (NMM) for the non-linear mapping of features from LR to HR. The FEM contains a convolutional layer and two Res ASPP Modules, expanding images into a high-dimensional feature space and increasing the receptive field, respectively. In the NMM, three FSABs are stacked, and the results of these FSABs are adaptively fused to fully leverage global multi-level features. Each FSAB employs an LF path for low-frequency features and an HF path for high-frequency features, with the LF path containing three densely connected Low-Frequency Attention Modules (LFAMs) and the HF path containing three densely connected High-Frequency Attention Modules (HFAMs). Within the HFAM, an HFAB and a Fusion Block are integrated, with the HFAB incorporating a projection error mechanism for processing high-frequency features. Similarly, the LFAM includes an LFAB and a Fusion Block for processing low-frequency features. To fully utilize informative features and enhance the details in image restoration, we introduce attention mechanisms in both the LFAB and HFAB.

In summary, the main contributions of the proposed image SR method are as follows:

- We introduce the novel deep convolutional neural network FSANet for image super-resolution tasks, utilizing a densely connected structure to leverage the powerful representational capability of deep CNNs and employing a parallel branching structure to separately process high- and low-frequency features.

- To further enhance the quality of the network's output images, we incorporate attention mechanisms in the LFAB and HFAB to fully exploit informative features across both channel and spatial dimensions.
- Experimental results demonstrate that our proposed method achieves higher performance compared to state-of-the-art super-resolution methods.

2. Related Work

There is a huge amount of work on image super-resolution, and thus, a comprehensive survey on SR methods is beyond the scope of this paper. This section provides a brief overview of some related works that are based on deep learning methods, frequency-separated networks, and attention networks.

2.1. Image Super-Resolution Based on Deep Learning

Compared to traditional mathematical methods, neural networks possess superior non-linear matching capabilities. SR methods based on deep learning include different usage scenarios, such as those based on classic blind image SR [3], non-blind image SR [19], real image SR [20], text-focused scene image SR [21], lightweight image SR [22], hyperspectral image SR [23], video SR [24], attenuation correction SR [25,26], etc. Dong et al. first introduced SRCNN [3], which contains three convolutional layers, to address super-resolution issues. To regularize the solution, CSCN [4] and SCN [5] integrate traditional sparse coding with deep learning, demonstrating the value of conventional methods in deep neural networks. Unlike networks that upscale LR images to an HR size before input, ESPCN [10] and FSRCNN [9] directly learn the mapping from LR to HR, effectively increasing the network's responsiveness. At the end of the network, the sub-pixel convolution and deconvolution layers are used to obtain SR images. This network structure significantly influenced the design of subsequent SR networks.

Vgg-net [27] indicates that deeper networks can perform more complex non-linear mappings, thereby enhancing the restoration of details in SR images. Since normalization in super-resolution networks can lead to artifacts and slow and unstable training, SR networks employ alternative methods to address the vanishing gradient problem, facilitating easier network training. Since LR and HR images share most fundamental features, VDSR [6] employs the residual learning of the differences between LR and HR images, not only increasing the network layers to 20 but also enhancing the network's convergence speed. MemNet [7] uses memory blocks containing recursive and gate units to address the issue of weakened information flow due to increased network depth. Unlike increasing the number of convolutional layers to deepen the network, DRCN [8] employs a very deep recursive layer to enhance the network's feature abstraction and parameter sharing, while recursive supervision and skip connections are used to mitigate the effects of network depth. Residual blocks [28] are used in networks [11,12] to address the vanishing gradient problem, further increasing network depth and representational capacity. To further increase network depth, Tong et al. [13] and Zhang et al. [16] directly connected the current layer with all subsequent layers using dense skip connections. This forms a contiguous memory mechanism, adaptively integrating information from multiple levels. Deep learning-based methods have shown exceptional performance in super-resolution tasks. The proposed method is based on deep learning.

2.2. Frequency-Separated Networks

To enhance training speed and performance, Zhao et al. [17] utilized deep convolutional networks and ResNet for high-frequency information storage and expanded the network's receptive field, increasing the accuracy of detail restoration in images. SRDN [18] employs a densely connected convolutional neural network for high-frequency information enhancement, increasing the learning rate for high-frequency areas to focus more on reconstructing high-frequency regions in images. SRFBN [29] consists of feedback blocks using a feedback mechanism, providing high-level information through a series of up-

and downsampling layers. FSN [30] divides image features into high and low frequencies for respective processing, employing Octave Convolution to maintain a good interaction between low- and high-frequency information. DBPN [31] introduces iterative upsampling and downsampling layers, where the Up-Projection Unit generates high-frequency features, and the Down-Projection Unit produces low-frequency features. Yang et al. [32] proposed a deep recursive low-frequency fusion network and designed a variance-based channel attention mechanism to make the information distribution of each feature map under different variances more reasonable. Refs. [17,18] only processed high-frequency features in images, overlooking the significance and importance of low-frequency features. In contrast, our method extracts both low- and high-frequency information. While we also focus on processing high-frequency features similar to [17,18], we do not neglect the processing of low-frequency features. This approach ultimately enhances the performance of the network.

2.3. Attention Networks

The attention mechanism offers a new perspective for task resolution, learning crucial information from inputs and demonstrating superiority in various computer vision tasks, such as object detection, image segmentation, and action recognition. The authors who proposed SCA-CNN [33] argued that previous spatial attention models only considered information within the CNN's spatial and multilayer contexts; hence, they introduced channel attention to discern which channels are most important for generating image captions. DANet [34] enhances context capture by adding positional and channel self-attention modules to model semantic relations in both the spatial and channel dimensions, resulting in finer scene segmentation outcomes. Zhang et al. [35] employed an attention mechanism for the selective integration of multi-level features, reducing background interference and enhancing object detection performance.

Liu et al. [36] used an attention mechanism to distinguish and enhance high-frequency information, improving detail restoration. LR images contain both low- and high-frequency information treated equally, thus diminishing detail restoration. Hence, RCAN [37] combines channel attention with residuals, allocating more computation to high-frequency information as network depth increases. Lu et al. [38] employed recursive units with channel attention to extract significant features from channels, using multi-level feature fusion techniques for feature enhancement. In CSFM [39], spatial and channel attention mechanisms, along with dense connections, are used to distinguish critical features across dimensions and mitigate the weakening of information flow in deep networks. The aforementioned works utilized attention mechanisms in super-resolution tasks but did not consider feature separation to alleviate the learning difficulty of attention mechanisms. By separating high- and low-frequency features in images and processing them differently, our approach enables attention mechanisms to focus on learning distinct features for backgrounds (low-frequency features) and complex texture features (high-frequency features) separately. This reduces the network's learning burden while enhancing its ability to distinguish between these two types of features.

3. Method

In order to use a densely connected structure to leverage the powerful representational capability of deep CNNs and separate process high- and low-frequency features, in this paper, we propose a Frequency-Separated Attention Network for image super-resolution, termed FSANet. First, we introduce the overall network architecture in Section 3.1. Second, we present the frequency-separated attention block in Section 3.2. Third, we describe the High-Frequency Attention Module in Section 3.3. And last, we present the Low-Frequency Attention Module in Section 3.4.

3.1. Network Architecture

As shown in Figure 1, our proposed FSANet consists of the Feature Extraction Module (FEM), Non-Linear Mapping Module (NMM), and Reconstruction Module (RM). We use I_{LR}, I_{SR}, and I_{HR} to denote the input, output, and high-resolution image of FSANet, respectively. In the FEM, I_{LR} is first passed through a convolution layer for feature extraction. The output g_{conv} is then processed by two Res ASPP Modules, each of which contains three parallel deep CNNs to expand the receptive field and obtain multi-scale features.

$$\begin{aligned} g_{K_2} &= f_{FEM}(I_{LR}) \\ &= f_{K_2}(f_{K_1}(f_{conv}(I_{LR})) + f_{conv}(I_{LR})) \\ &= f_{K_2}(g_{K_1} + g_{conv}). \end{aligned} \tag{1}$$

Here, $f_{FEM}(\cdot)$ denotes the FEM, and $f_{conv}(\cdot)$ represents the 3×3 convolution producing g_{conv}. $f_{K_1}(\cdot)$ and $f_{K_2}(\cdot)$ denote two Res ASPP Modules with the outputs g_{K_1} and g_{K_2}, respectively.

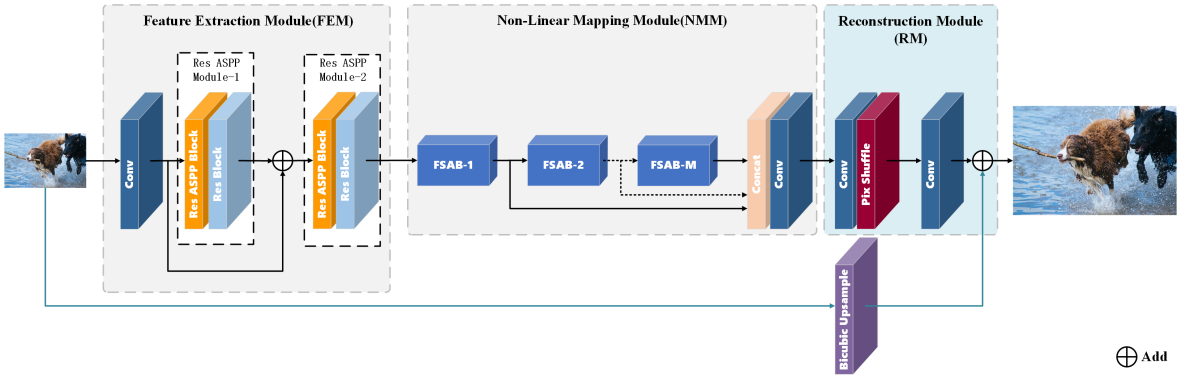

Figure 1. The architecture of the proposed FSANet. The basic modules of deep CNNs are used in the Res ASPP Module and NMM.

In the NMM, three FSABs are linearly stacked. Assuming that the input of the m-th FSAB is F_{m-1} and its output is F_m, then the input for the first FSAB is F_0 (i.e., g_{K_2}), and the output of the last FSAB is F_M. The m-th FSAB is as follows:

$$F_m = f^m_{FSAB}\left(f^{m-1}_{FSAB}\left(\cdots f^1_{FSAB}(F_0)\right)\right). \tag{2}$$

Here, $f^m_{FSAB}(\cdot)$ represents the m-th FSAB. Each FSAB outputs distinct features. To fully utilize these hierarchical features, we adopt an adaptive fusion of long-term multi-level features, concatenating the outputs of the three FSABs before feeding them into a convolution layer. Thus, the NMM is as follows:

$$\begin{aligned} g_{NMM} &= f_{NMM}(F_0) \\ &= \varphi_{conv}([F_1, F_2, \cdots, F_M]). \end{aligned} \tag{3}$$

Here, $f_{NMM}(\cdot)$ denotes the NMM, $\varphi_{conv}(\cdot)$ represents the 3×3 convolution yielding g_{NMM}, and $[\cdot]$ signifies the feature concatenation operation.

In the RM, we employ convolution and sub-pixel convolution layers [10] for upsampling to obtain I_{SR}. Additionally, we utilize a global skip connection through bicubic upsampling to maintain long-term memory.

$$\begin{aligned} I_{SR} &= f_{RM}(g_{NMM}) + Bicubic(I_{LR}) \\ &= f_{RM}(f_{NMM}(f_{FEM}(I_{LR}))) + Bicubic(I_{LR}), \end{aligned} \tag{4}$$

where $f_{RM}(\cdot)$ denotes the RM, and $Bicubic(\cdot)$ represents the bicubic upsampling operation.

According to [16], the Peak Signal-to-Noise Ratio (PSNR) is highly correlated with the pixel-wise differences between I_{SR} and I_{HR}. Given that the L_2 loss function tends to emphasize larger differences and weaken smaller ones, and considering that its convergence is inferior to that of the L_1 loss function, we use the L_1 loss function to optimize FSANet. Given a set of training patch pairs $\{I^i_{LR}, I^i_{HR}\}^I_{i=1}$, the loss function of FSANet is as follows:

$$L(\theta) = \frac{1}{I}\sum_{i=1}^{I}\left\|F_{FSANet}\left(I^i_{LR}\right) - I^i_{HR}\right\|_1, \tag{5}$$

where $F_{FSANet}(\cdot)$ denotes FSANet, and θ represents the parameters within FSANet.

3.2. Frequency-Separated Attention Block

The extracted high-frequency features, compared to low-frequency features, contain more information and thus require more processing, for which we propose the FSAB. As shown in Figure 2, the m-th FSAB consists of two branches: a high-frequency path (HF path) formed by three HFAMs to process high-frequency features and a low-frequency path (LF path) formed by a linear stack of LFAMs to process low-frequency features.

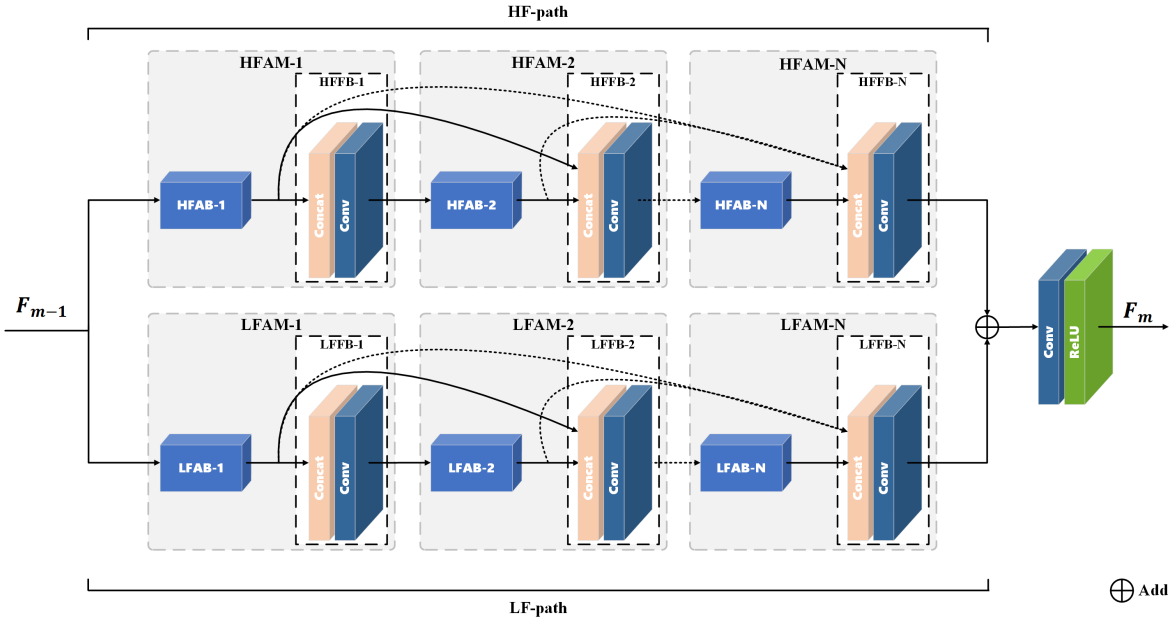

Figure 2. The architecture of the m-th FSAB.

H_{in_n} represents the input to the n-th HFAB, while H_{out_n} represents the output. There are a total of N HFABs. The equation is given by

$$H_{out_n} = f^n_{HFAB}\left(H_{in_n}\right). \tag{6}$$

Here, $f^n_{HFAB}(\cdot)$ represents the n-th HFAB, which is detailed in Section 3.3. The expression for the n-th High-Frequency Fusion Block (HFFB) is as follows:

$$F^n_{HFFB} = f^n_{HFFB}\left(\left[H_{out_1}, \cdots, H_{out_n}\right]\right), \tag{7}$$

where $f^n_{HFFB}(\cdot)$ denotes the convolution in the n-th HFFB, with its output being F^n_{HFFB}.

In the LF path, let L_{in_n} be the input and L_{out_n} be the output of the n-th LFAB:

$$L_{out_n} = f^n_{LFAB}\left(L_{in_n}\right). \tag{8}$$

$f^n_{LFAB}(\cdot)$ represents the n-th LFAB, which is emphasized in Section 3.4. To achieve relatively high performance, we use Low-Frequency Fusion Blocks (LFFBs) for multi-level dense

local feature fusion by directly connecting the output of the current and previous LFABs to the LFFB. Consequently, the expression for the n-th LFFB is as follows:

$$F_{LFFB}^{n} = f_{LFFB}^{n}\left(\left[L_{out_1}, \cdots, L_{out_n}\right]\right). \tag{9}$$

$f_{LFFB}^{n}(\cdot)$ represents the n-th LFFB, with its output denoted by F_{LFFB}^{n}.

Finally, the outputs of both branches are added to merge high-frequency and low-frequency information. The output of the FSAB is generated through a deep CNN to complement the advantages of high- and low-frequency features. The m-th FSAB is as follows:

$$\begin{aligned} F_m &= f_{FSAB}^{m}(F_{m-1}) \\ &= ReLU\left(\phi\left(F_{LFFB}^{N} + F_{HFFB}^{N}\right)\right) \\ &= ReLU\left(\phi\left(f_{LFFB}^{N}\left(\left[L_{out_1}, \cdots, L_{out_N}\right]\right) + f_{HFFB}^{N}\left(\left[H_{out_1}, \cdots, H_{out_N}\right]\right)\right)\right), \end{aligned} \tag{10}$$

Here, $\phi(\cdot)$ represents the convolution, and $ReLU(\cdot)$ indicates the ReLU layer.

3.3. High-Frequency Attention Module

In this section, we introduce two parts (the architectures of the HFAB and the High-Frequency Block) of the High-Frequency Attention Module in detail.

3.3.1. The Architecture of the HFAB

As illustrated in Figure 3, the HFAB primarily comprises three components: a linear stack of High-Frequency Blocks (HFBs), a Frequency Fusion Block, and a CSA Module. Let the input of the t-th HFB be F_{HFB}^{t-1} and the output be F_{HFB}^{t}. Thus, the t-th HFB can be defined as follows:

$$F_{HFB}^{t} = f_{HFB}^{t}\left(f_{HFB}^{t-1}\left(\ldots f_{HFB}^{1}\left(F_{HFB}^{0}\right)\right)\right), \tag{11}$$

where $f_{HFB}^{t}(\cdot)$ represents the t-th HFB. In the experiment, $t \in \{1, 2, 3\}$.

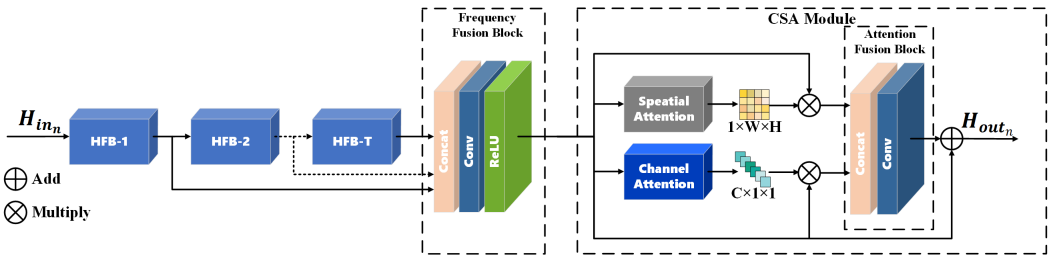

Figure 3. The architecture of the n-th HFAB.

As the network deepens, the features within each HFB layer differ. To fully utilize this information, we employ a Frequency Fusion Block for multi-level local feature fusion. The Frequency Fusion Block selectively fuses the outputs from the preceding HFB by utilizing a Concat layer and processing them through a deep CNN. The result F_{FreF} serves as the input for the CSA Module and is defined as follows:

$$\begin{aligned} F_{FreF} &= f_{FreF}([F_{HFB}^{1}, \cdots, F_{HFB}^{T}]) \\ &= ReLU(\psi([F_{HFB}^{1}, \cdots, F_{HFB}^{T}])), \end{aligned} \tag{12}$$

where $f_{FreF}(\cdot)$ denotes the Frequency Fusion Block, and $\psi(\cdot)$ represents the convolution in the Frequency Fusion Block.

Distinct features play varied roles in image reconstruction. To enhance the network's sensitivity to crucial features, we utilize a CSA Module [39] incorporating channel attention and spatial attention to selectively strengthen features in both the channel and spatial dimensions. Spatial attention, in particular, aids in distinguishing between smooth areas and texture features. Within the CSA Module, features modified by attention mechanisms

are adaptively fused and then skip-connected with the original features, thus selectively enhancing features without losing information from the original ones. The n-th HFAB can be defined as follows:

$$\begin{aligned} H_{out_n} &= f^n_{HFAB}(H_{in_n}) \\ &\doteq f_{CSAM}(F_{FreF}) \\ &= f_{AttF}([f_{SA}(F_{FreF}) \otimes F_{FreF}, f_{CA}(F_{FreF}) \otimes F_{FreF}]) + F_{FreF}, \end{aligned} \tag{13}$$

where $f_{CSAM}(\cdot)$ denotes the CSA Module, $f_{SA}(\cdot)$ [39] and $f_{CA}(\cdot)$ [39] represent spatial attention and channel attention, respectively, and $f_{AttF}(\cdot)$ is the convolution function within the Attention Fusion Block.

3.3.2. The Architecture of the HFB

In D-DBPN [31], an iterative error-correcting feedback mechanism was introduced, and Timoft et al. [40] demonstrated that high-frequency information can be progressively refined by continuously subtracting the results of upsampling and downsampling from the original input. To better process high-frequency features, a deep CNN is applied in the middle of down- and upsampling. To reduce the degradation of the original information after one iteration of refinement, a residual block is added. F^{t-1}_{HFB} and F^{t}_{HFB} are defined as the input and output of the t-th HFB, respectively, with down- and upsampling specified as follows:

$$\begin{aligned} F_{project} &= f_{project}(F^{t-1}_{HFB}) \\ &= ReLU(f_{down}(ReLU(f_{conv}(RELU(f_{up}(F^{t-1}_{HFB})))))). \end{aligned} \tag{14}$$

$F_{project}$ and $f_{project}(\cdot)$ represent the output and function of down- and upsampling [31], respectively. Here, $f_{up}(\cdot)$ is the function for deconvolution operations, and both $f_{conv}(\cdot)$ and $f_{down}(\cdot)$ represent convolution operations. The HFB can be defined as follows:

$$\begin{aligned} F^{t}_{HFB} &= f_{HFB}(F^{t-1}_{HFB}) \\ &= f_{resblock}(f_{project}(F^{t-1}_{HFB}) - F^{t-1}_{HFB}). \end{aligned} \tag{15}$$

Here, $f_{resblock}(\cdot)$ is the function for the residual block [28], as illustrated in Figure 4.

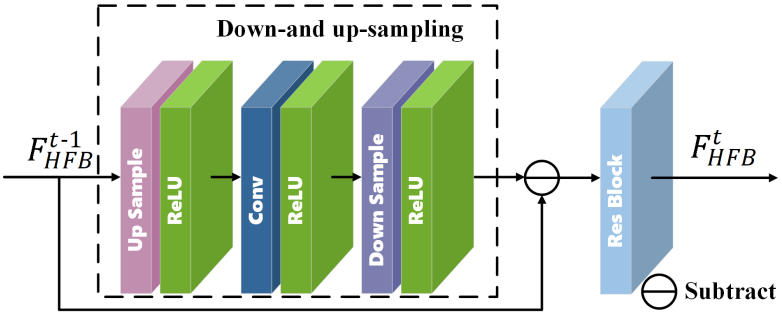

Figure 4. The architecture of the t-th HFB.

3.4. Low-Frequency Attention Module

We utilize the Low-Frequency Attention Block (LFAB) to process low-frequency features, employing a tri-branch structure for handling the low-frequency features L_{in_n}, as illustrated in Figure 5. One branch retains the original input information, corresponding to the middle branch in Figure 5. Another branch utilizes a deep CNN and a convolutional layer with a kernel size of 3×3, depicted as the top branch in Figure 5. The final branch comprises a deep CNN and a convolutional layer with a kernel size of 5×5 to expand the field of view, shown as the bottom branch in Figure 5. To mitigate the impact of increased network depth on feature attenuation and selective enhancement across different chan-

nels, we perform an additive operation on the three branches before passing the result through a residual block and a channel attention mechanism to obtain the output L_{out_n} of the t-th LFAB,

$$\begin{aligned} L_{out_n} &= f^n_{LFAB}\left(L_{in_n}\right) \\ &= f_{branchres}(L_{in_n}) \otimes f_{CA}\left(f_{branchres}(L_{in_n})\right) \\ &= F_{branchres} \otimes f_{CA}(F_{branchres}), \end{aligned} \tag{16}$$

where $f_{branchres}(\cdot)$ denotes the tri-branch and a Res Block in Figure 5, and $f_{CA}(\cdot)$ [39] represents channel attention.

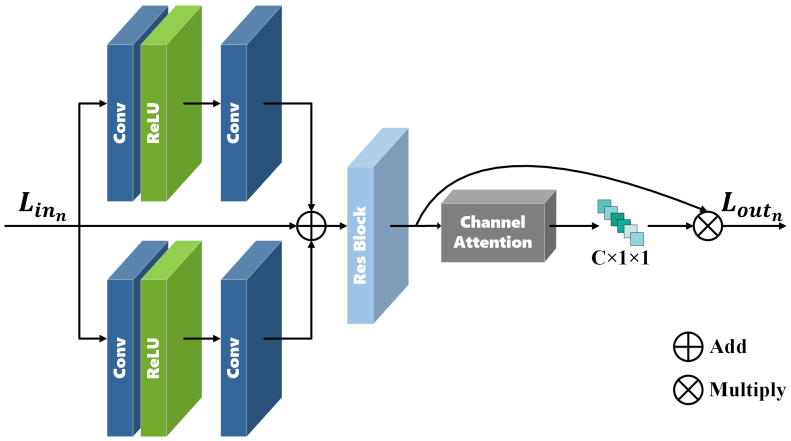

Figure 5. The architecture of the n-th LFAB.

4. Experiments

In this section, we first conduct an ablation study to validate the effectiveness of the proposed FSANet network architecture. Then, we compare FSANet with several other networks on benchmark datasets in terms of the PSNR and SSIM. We follow the approach of previous work [39] to train and test our model. We use the DIV2K [40] dataset, which contains 800 high-quality images, for training.

4.1. Settings

In this section, we present the datasets, metrics, and implementation details.

4.1.1. Datasets and Metrics

We train and test our network following methods in prior work [16]. LR images in DIV2K are obtained by bicubic downsampling of HR images by factors of ×2, ×3, and ×4. We evaluate our model on widely used benchmark datasets: Set5 [41], Set14 [42], BSD100 [43], Urban100 [44], and Manga109 [45], which contain 5, 14, 100, 100, and 109 images, respectively, covering common scenes from daily life. The model evaluation metrics include the Peak Signal-to-Noise Ratio (PSNR) and Structural Similarity Index Measure (SSIM) [46], with results computed on the Y channel (i.e., luminance) of the YCbCR space. Higher PSNR and SSIM values closer to 1 indicate better quality of the reconstructed SR images.

4.1.2. Implementation Details

During training, data augmentation is performed through random vertical and horizontal flips and 90° rotations around the image center, with a mini-batch size of 16 and the random cropping of 64 × 64 patches from LR images for input. Following the method in [39], the input to the model is normalized by subtracting the mean RGB values of DIV2K to highlight individual feature differences, and the mean RGB values of DIV2K are added back before the network output. We use the ADAM optimizer with an initial learning rate of 10^{-4} to train the

network, halving the learning rate after 1.5×10^5 and 2×10^5 iterations. We implement FSANet using PyTorch and conduct training and testing on an NVIDIA RTX 3090 GPU.

The Res ASPP Block [47] includes three dilated convolutions with dilation rates of 1, 4, and 8. In RM, the first convolutional layer has filters of 256, 576, and 1024 for magnification factors of ×2, ×3, and ×4, respectively. The second layer has 3 filters. And all other layers have 64 filters each. The values of N and M are both set to 3. The reduction ratio in channel attention is 16, and the increase ratio in spatial attention is 2.

4.2. Ablation Study

In this section, we show the effectiveness of Res ASPP feature extraction, frequency-separated structures, and attention mechanisms.

4.2.1. The Effectiveness of Res ASPP Feature Extraction

We utilized the Res ASPP Module to enhance the field of view for improved feature extraction. To verify the effectiveness of the Res ASPP Module, we conducted the following experiments: (1) removing the Res ASPP Module from the FEM; (2) retaining the Res ASPP Module within the FEM. As shown in Figure 6, we visualized the average feature maps after feature extraction from both experiments. The outputs of feature extraction were as follows: for experiment (1), the result of the first convolution g_{conv} in the Feature Extraction Module, and for experiment (2), the results of the first convolution g_{conv} and the output of Res ASPP Module-2 g_{K_2}. From the feature maps, it is evident that the contours of the feature maps without the Res ASPP Module are discontinuous and blurred. This could be due to misinterpreting adjacent similar features as dissimilar or vice versa within a limited field of view. Based on the test results on the benchmark dataset outlined in Table 1, the outcomes without the Res ASPP Module consistently underperform compared to those with it, thereby validating the effectiveness of the Res ASPP Module. Moreover, as evident from Figure 7a, the utilization of the Res ASPP Module accelerates the convergence of the network during training by enhancing feature extraction.

(**a**) g_{conv} (**b**) g_{conv} (**c**) g_{K_2}

Figure 6. To explore the impact of the Res ASPP Module, it was removed from the FEM, followed by retraining. A comparison was made between the feature extraction results of the network with and without the Res ASPP Module. (**a**) illustrates the feature map of the output g_{conv} (in Equation (1)) without utilizing the Res ASPP Module. (**b**) and (**c**) depict the feature maps of g_{conv} (in Equations (1)) and g_{K_2} (in Equation (1)), respectively, with the utilization of the Res ASPP Module within FEM. The features regarding the wings and head are slightly blurrier in (**a**) compared to (**b**) and (**c**).

Table 1. Test results on the standard dataset without and with the use of the Res ASPP Module.

Dataset	Deactivate Res ASPP Module PSNR/SSIM	Activate Res ASPP Module PSNR/SSIM
Set5	38.19/0.9610	**38.20/0.9612**
Set14	33.79/0.9190	**33.88/0.9200**
BSD100	32.29/0.9009	**32.33/0.9016**
Urban100	32.69/0.9337	**32.83/0.9351**
Manga109	39.03/0.9778	**39.11/0.9781**

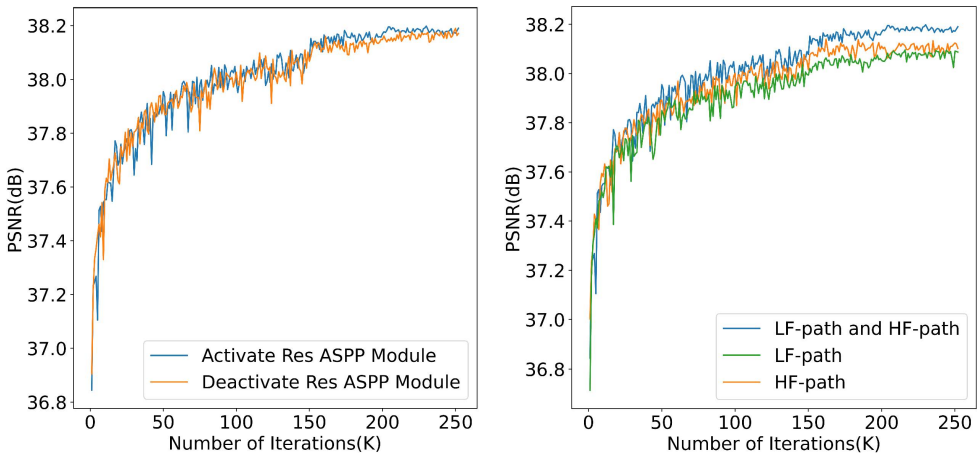

Figure 7. (**a**,**b**) showcase the PSNR test results on the benchmark dataset Set5. (**a**) represents the results with and without utilizing the Res ASPP Module, while (**b**) illustrates the outcomes when employing both LF path and HF path simultaneously, only LF path, and only HF path.

4.2.2. The Effectiveness of Frequency-Separated Structures

The FSAB consists of an LF path (for low-frequency information) and an HF path (for high-frequency information).

In Figures 8 and 9, we visualize the average feature maps of low- and high-frequency information from the first three FSABs. The low-frequency information feature maps depict the general contours, while the high-frequency information feature maps describe the edges and textures. To verify the effectiveness of separating high- and low-frequency structures, we conducted the following experiments: (1) the FSAB containing only the LF path, (2) the FSAB containing only the HF path, (3) the FSAB containing both the LF path and HF path. To roughly maintain equal parameters, the first two experiments used 13 and 4 FSABs, respectively.

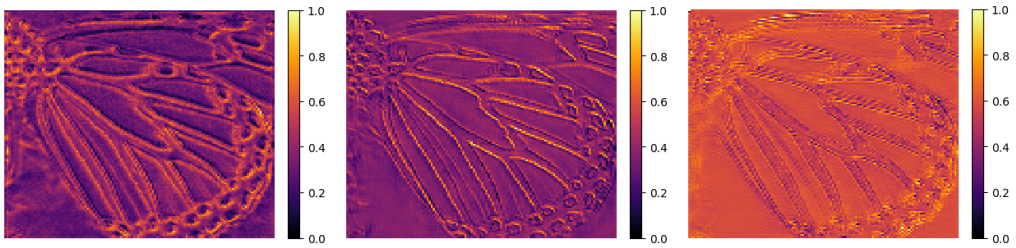

Figure 8. LFAB-1, **LFAB-2**, and **LFAB-3** are the feature maps corresponding to the first, second, and third FSAB outputs in the LF path.

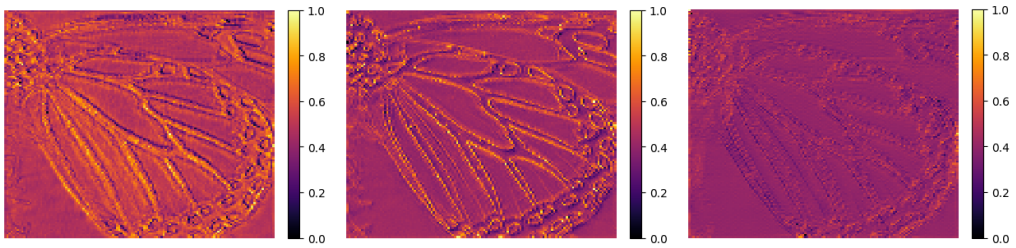

Figure 9. HFAB-1, **HFAB-2**, and **HFAB-3** are the feature maps corresponding to the first, second, and third FSAB outputs in the HF path.

Figure 7b displays the PSNR results of the three experiments tested on the Set5 dataset during the training process, and Table 2 shows the test results of the three experiments on standard datasets. We found that using both the LF path and HF path for image reconstruction yielded better results and faster convergence than using either path alone.

Table 2. The test results of three experiments on the standard dataset.

Dataset	LF Path PSNR/SSIM	HF Path PSNR/SSIM	LF Path and HF Path PSNR/SSIM
Set5	38.09/0.9608	38.15/0.9609	**38.20/0.9612**
Set14	33.78/0.9192	33.73/0.9186	**33.88/0.9200**
BSD100	32.24/0.9004	32.26/0.9005	**32.33/0.9016**
Urban100	32.46/0.9315	32.57/0.9324	**32.83/0.9351**
Manga109	38.91/0.9776	38.98/0.9777	**39.11/0.9781**

4.2.3. The Effectiveness of Attention Mechanisms

To verify the effectiveness of attention mechanisms, we removed all attention modules from the LF path and HF path in the original model and retrained it. As shown in Figure 10, we extracted the average feature maps from the LF path and HF path both with and without attention modules. The figures reveal that in the LF path, contours (low-frequency information) are highlighted in the feature maps. However, the use of attention causes the LF path to focus more on low-frequency information, making the texture areas (high-frequency information) with attention dimmer than those without. In the HF path, textures (high-frequency information) are highlighted, and the use of attention ensures that similar textures (high-frequency information) are processed similarly. As indicated in Table 3, we also conducted tests on standard datasets and found that the results with attention modules are better than those without.

Table 3. Test results on the benchmark dataset for models without and with the attention module.

Dataset	Deactivate Attention PSNR/SSIM	Activate Attention PSNR/SSIM
Set5	38.16/0.9609	**38.20/0.9612**
Set14	33.78/0.9190	**33.88/0.9200**
BSD100	32.28/0.9009	**32.33/0.9016**
Urban100	32.68/0.933	**32.83/0.9351**
Manga109	39.02/0.9779	**39.11/0.9781**

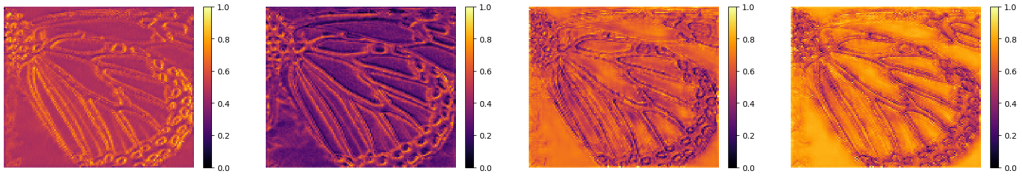

(**a**) (**b**) (**c**) (**d**)

Figure 10. Visualizations of feature maps for the LF path and the HF path are presented. (**a**) displays the feature map without attention in the LF path, while (**b**) exhibits the feature map with attention in the LF path. (**c**) showcases the feature map without attention in the HF path, and (**d**) illustrates the feature map with attention in the HF path.

4.3. Comparison with State-of-the-Art Methods

In this section, we show the visualization of PSNR and SSIM results and the analysis results of model comparisons.

4.3.1. Comparison and Visualization of PSNR and SSIM Results

In this section, we compare our FSANet with state-of-the-art methods, including SRCNN [3], FSRCNN [9], VDSR [6], HDRN [48], CARN [49], MemNet [7], IMDN [50], LAPAR-A [51], SRMD [52], A2F-L [53], and FENet [54].

Table 4 presents the values of the PSNR and SSIM metrics for different networks at magnification factors of ×2, ×3, and ×4 on five benchmark datasets commonly used in super-resolution. Figure 11 displays a visual quality comparison of image reconstructions at a magnification factor of 4×. The images reconstructed by FSANet exhibit more vivid details compared to those from other networks, as shown in the figures.

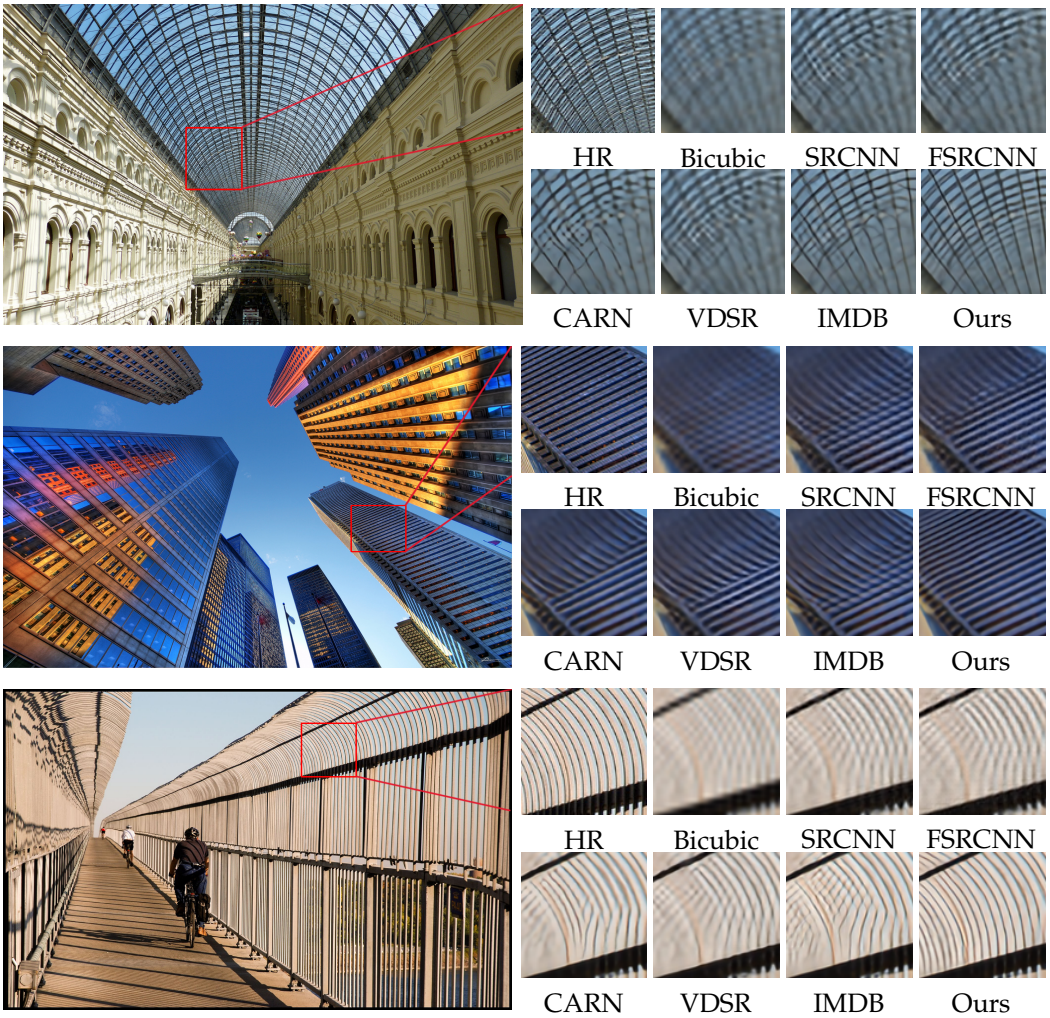

Figure 11. A qualitative comparison of classic state-of-the-art SR models for the ×4 upscaling task. Ours (FSANet) can restore more accurate and sharper details than the other models. We crop the SR image according to the position of the red box to clearly show the details. On the far left is the ground-truth image, while the images labeled "HR" on the right represent cropped portions of the ground-truth image.

Table 4. Quantitative evaluations of the proposed FSANet against state-of-the-art methods on commonly used benchmark datasets. The best results are marked in bold. "–/–" indicates that the corresponding method does not provide results.

Method	Scale	Set5	Set14	BSD100	Urban100	Manga109
		PSNR/SSIM	PSNR/SSIM	PSNR/SSIM	PSNR/SSIM	PSNR/SSIM
Bicubic	×2	33.68/0.9304	30.24/0.8691	29.56/0.8453	26.88/0.8405	30.80/0.9399
SelfExSR	×2	36.50/0.9537	32.23/0.9036	31.18/0.8855	29.38/0.9032	–/–
Laplacian	×2	25.91/0.8200	24.31/0.7825	24.19/0.7653	22.10/0.7643	24.19/0.8422
SRCNN	×2	36.66/0.9542	32.45/0.9067	31.36/0.8879	29.51/0.8946	35.60/0.9663
FSRCNN	×2	36.98/0.9556	32.62/0.9087	31.50/0.8904	29.51/0.8946	35.67/0.9710
VDSR	×2	37.53/0.9587	33.05/0.9127	31.90/0.8904	30.77/0.9141	37.22/0.9750
HDRN	×2	37.75/0.9590	33.49/0.9150	32.03/0.8980	31.87/0.9250	38.07/0.9770
CARN	×2	37.76/0.9590	33.52/0.9166	32.09/0.8978	31.92/0.9256	38.36/0.9764
MemNet	×2	37.78/0.9597	33.28/0.9142	32.08/0.8978	31.31/0.9195	37.72/0.9740
SRMD	×2	37.79/0.9601	33.32/0.9159	32.05/0.8985	31.33/0.9204	38.07/0.9761
IMDN	×2	38.00/0.9605	33.63/0.9177	32.19/0.8996	32.17/0.9283	38.88/0.9774
LAPAR-A	×2	38.01/0.9605	33.62/0.9183	32.19/0.8999	32.10/0.9283	38.67/0.9772
A2F-L	×2	38.09/0.9607	33.78/0.9192	32.23/0.9002	32.46/0.9313	38.95/0.9772
FENet	×2	38.08/0.9608	33.70/0.9184	32.20/0.9001	32.18/0.9287	38.89/0.9775
Ours	×2	**38.20/0.9612**	**33.88/0.9200**	**32.33/0.9016**	**32.83/0.9351**	**39.11/0.9781**
Bicubic	×3	30.40/0.8686	27.54/0.7741	27.21/0.7389	24.46/0.7349	26.95/0.8556
SelfExSR	×3	32.62/0.9094	29.16/0.8197	28.30/0.7843	–/–	–/–
Laplacian	×3	25.29/0.7246	24.03/0.6718	24.02/0.6496	21.77/0.6485	23.77/0.7616
SRCNN	×3	32.75/0.9090	29.29/0.8215	28.41/0.7863	26.24/0.7991	30.48/0.9117
FSRCNN	×3	33.16/0.9140	29.42/0.8242	28.52/0.7893	26.41/0.8064	31.10/0.9210
VDSR	×3	33.66/0.9213	29.78/0.8318	28.83/0.7976	27.14/0.8279	32.01/0.9340
HDRN	×3	34.24/0.9240	30.23/0.8400	28.96/0.8040	27.93/0.8490	33.17/0.9420
CARN	×3	34.29/0.9255	30.29/0.8407	29.06/0.8034	28.06/0.8493	33.49/0.9440
MemNet	×3	34.09/0.9248	30.00/0.8350	28.96/0.8001	27.56/0.8376	32.51/0.9369
SRMD	×3	34.12/0.9254	30.04/0.8382	28.97/0.8025	27.57/0.8398	33.00/0.9403
IMDN	×3	34.36/0.9270	30.32/0.8417	29.09/0.8046	28.17/0.8519	33.61/0.9445
LAPAR-A	×3	34.36/0.9267	30.34/0.8421	29.11/0.8054	28.15/0.8523	33.51/0.9441
A2F-L	×3	34.54/0.9283	30.41/0.8436	29.14/0.8062	28.40/0.8574	33.83/0.9463
FENet	×3	34.40/0.9273	30.36/0.8422	29.12/0.8060	28.17/0.8524	33.52/0.9444
Ours	×3	**34.64/0.9299**	**30.51/0.8456**	**29.21/0.8078**	**28.70/0.8633**	**34.04/0.9474**
Bicubic	×4	28.43/0.8109	26.00/0.7023	25.96/0.6678	23.14/0.6574	24.89/0.7866
SelfExSR	×4	30.33/0.8623	27.40/0.7518	26.85/0.7108	24.82/0.7386	–/–
Laplacian	×4	27.22/0.7544	25.41/0.6772	25.46/0.6492	22.71/0.6358	24.44/0.7567
SRCNN	×4	30.48/0.8628	27.50/0.7513	26.90/0.7103	24.52/0.7226	27.58/0.8555
FSRCNN	×4	30.70/0.8657	27.59/0.7535	26.96/0.7128	24.60/0.7258	27.90/0.8610
VDSR	×4	31.25/0.8838	28.02/0.7678	27.29/0.7252	25.18/0.7525	28.83/0.8870
HDRN	×4	32.23/0.8960	28.58/0.7810	27.53/0.7370	26.09/0.7870	30.43/0.9080
CARN	×4	32.13/0.8937	28.60/0.7806	27.58/0.7349	26.07/0.7837	30.40/0.9082
MemNet	×4	31.74/0.8893	28.26/0.7723	27.40/0.7281	25.50/0.7630	29.42/0.8942
SRMD	×4	31.96/0.8925	28.35/0.7787	27.49/0.7337	25.68/0.7731	30.09/0.9024
IMDN	×4	32.21/0.8948	28.58/0.7811	27.56/0.7353	26.04/0.7838	30.45/0.9075
LAPAR-A	×4	32.15/0.8944	28.61/0.7818	27.61/0.7366	26.14/0.7871	30.42/0.9074
A2F-L	×4	32.32/0.8964	28.67/0.7839	27.62/0.7379	26.32/0.7931	30.72/0.9115
FENet	×4	32.24/0.8961	28.61/0.7818	27.63/0.7371	26.20/0.7890	30.46/0.9083
Ours	×4	**32.37/0.8969**	**28.72/0.7842**	**27.66/0.7385**	**26.49/0.7977**	**30.80/0.9118**

4.3.2. Analysis of Model Comparisons

As illustrated in Figure 12a, we compared the super-resolution performance and parameter count of our FSANet at a magnification factor of ×2 with existing models, namely, VDSR [6], HDRN [48], CARN [49], IMDN [50], RDN [16], and EDSR [12]. Our network performs comparably to EDSR [12] and RDN [16], yet it requires significantly fewer parameters than EDSR [12] and slightly fewer than RDN [16]. Equally important

is the computational complexity. Our proposed FSANet for a scale factor of 2 has a computational burden of 150G Flops. We compared this computational burden with that of other methods and plot the results in Figure 12b. On the x-axis of Figure 12b, we represent the computational burden, while on the y-axis, we depict the performance on the benchmark dataset BSD100. As shown in Figure 12b, although our performance is slightly weaker than that of RDN [16], our computational complexity is significantly lower than that of RDN [16].

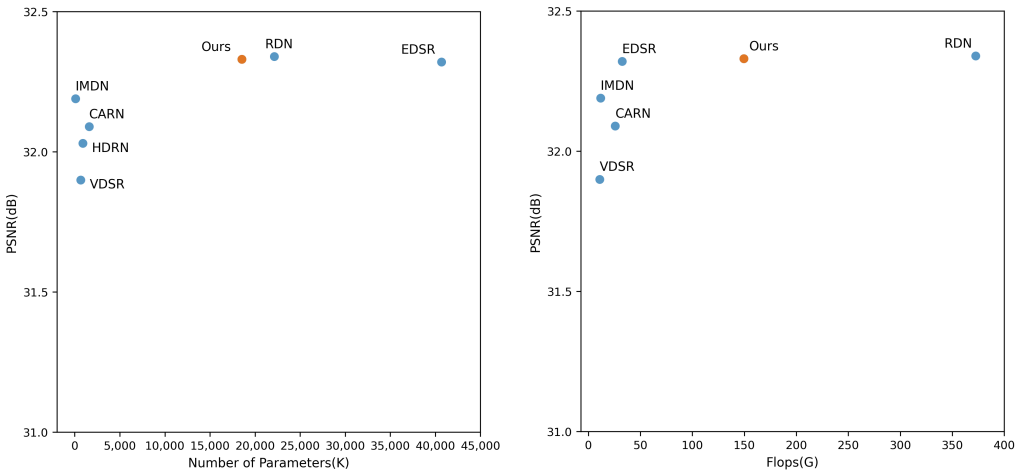

Figure 12. The graph in (**a**) illustrates the comparison between image restoration quality and network parameter count, while that in (**b**) depicts the comparison between image restoration quality and network computational burden.

4.3.3. Comparison with Other Methods on Real-World Images

Our model is designed specifically for the restoration of low-resolution images that have been downsampled using bicubic interpolation. In real-world scenarios, images may exhibit noise, sensor damage, compression artifacts, and other imperfections. As shown in Figure 13, the processed images still retain some level of blurriness and may not exhibit significant visual differences compared to other methods. However, we conducted tests on the RealSR [55] and DrealSR [56] real-world datasets, evaluating the PSNR and SSIM metrics for a magnification factor of 4. As demonstrated in Table 5, our network performs slightly better than other methods.

Table 5. The test results on benchmark datasets for real-world super-resolution at a magnification factor of ×4.

Dataset	DRealSR PSNR/SSIM	RealSR PSNR/SSIM
Bicubic	30.78/0.8468	27.30/0.7557
SRCNN	30.88/0.8490	27.65/0.7711
FSRCNN	30.79/0.8473	27.65/0.7692
CRAN	30.82/0.8474	27.66/0.7700
VDSR	30.82/0.8458	27.52/0.7554
IMDN	30.80/0.8489	27.66/0.7717
Ours	**31.47/0.8580**	**27.77/0.7739**

Figure 13. Visualization results on a real-world super-resolution benchmark dataset.

5. Conclusions

This work introduces a novel attention-integrated module, the FSAB, for separating low-frequency and high-frequency features. This module employs a parallel dual-branch structure for processing high-frequency and low-frequency features, focusing the network on high-frequency features to enhance detail restoration in images. It also uses local dense connections and channel and spatial mechanisms to fully exploit heuristic features. The test results on several benchmark datasets demonstrate the effectiveness of our proposed network structure. Our experiments also show that the ASPP structure used in the super-resolution field can effectively extract features, and our work confirms the effectiveness of attention networks with frequency-separated structures for super-resolution problems. We hope our work offers the computer vision community a new perspective on addressing super-resolution tasks.

There are still some limitations of the proposed network, which has a large number of parameters and is difficult to run on constrained edge devices. Mobile phone users have a desire for image super-resolution processing, but there is not much research in this area, so lightweight super-resolution on mobile phones is a very promising direction. At the same time, the proposed method is only suitable for bicubic downsampling, but real-

world images contain more complex noise, so super-resolution in real-world scenes is another challenge.

Author Contributions: Conceptualization, D.Q. and R.Y.; methodology, D.Q. and L.L.; validation, D.Q. and L.L.; formal analysis, D.Q.; investigation, L.L.; resources, L.L.; data curation, D.Q.; writing—original draft preparation, D.Q.; writing—review and editing, L.L. and R.Y.; visualization, L.L. All authors have read and agreed to the published version of the manuscript.

Funding: This work was supported in part by the Xuzhou Key Research and Development Program under Grant KC22287.

Institutional Review Board Statement: Not applicable.

Informed Consent Statement: Not applicable.

Data Availability Statement: The original contributions presented in the study are included in this article. Further inquiries can be directed to the corresponding author.

Conflicts of Interest: The authors declare no conflicts of interest.

References

1. Lu, X.; Yuan, H.; Yan, P.; Yuan, Y.; Li, X. Geometry constrained sparse coding for single image super-resolution. In Proceedings of the 2012 IEEE Conference on Computer Vision and Pattern Recognition, Providence, RI, USA, 16–21 June 2012; pp. 1648–1655.
2. Gao, X.; Zhang, K.; Tao, D.; Li, X. Image super-resolution with sparse neighbor embedding. *IEEE Trans. Image Process.* **2012**, *21*, 3194–3205.
3. Dong, C.; Loy, C.C.; He, K.; Tang, X. Image super-resolution using deep convolutional networks. *IEEE Trans. Pattern Anal. Mach. Intell.* **2015**, *38*, 295–307. [CrossRef] [PubMed]
4. Liu, D.; Wang, Z.; Wen, B.; Yang, J.; Han, W.; Huang, T.S. Robust single image super-resolution via deep networks with sparse prior. *IEEE Trans. Image Process.* **2016**, *25*, 3194–3207. [CrossRef] [PubMed]
5. Wang, Z.; Liu, D.; Yang, J.; Han, W.; Huang, T. Deep networks for image super-resolution with sparse prior. In Proceedings of the IEEE International Conference on Computer Vision, Santiago, Chile, 7–13 December 2015; pp. 370–378.
6. Kim, J.; Lee, J.K.; Lee, K.M. Accurate image super-resolution using very deep convolutional networks. In Proceedings of the IEEE Conference on Computer Vision and Pattern Recognition, Las Vegas, NV, USA, 27–30 June 2016; pp. 1646–1654.
7. Tai, Y.; Yang, J.; Liu, X.; Xu, C. Memnet: A persistent memory network for image restoration. In Proceedings of the IEEE International Conference on Computer Vision, Venice, Italy, 22–29 October 2017; pp. 4539–4547.
8. Kim, J.; Lee, J.K.; Lee, K.M. Deeply-recursive convolutional network for image super-resolution. In Proceedings of the IEEE Conference on Computer Vision and Pattern Recognition, Las Vegas, NV, USA, 27–30 June 2016; pp. 1637–1645.
9. Dong, C.; Loy, C.C.; Tang, X. Accelerating the super-resolution convolutional neural network. In Proceedings of the Computer Vision–ECCV 2016: 14th European Conference, Amsterdam, The Netherlands, 11–14 October 2016; Proceedings, Part II 14; Springer: Berlin/Heidelberg, Germany, 2016; pp. 391–407.
10. Shi, W.; Caballero, J.; Huszár, F.; Totz, J.; Aitken, A.P.; Bishop, R.; Rueckert, D.; Wang, Z. Real-time single image and video super-resolution using an efficient sub-pixel convolutional neural network. In Proceedings of the IEEE Conference on Computer Vision and Pattern Recognition, Las Vegas, NV, USA, 27–30 June 2016; pp. 1874–1883.
11. Tai, Y.; Yang, J.; Liu, X. Image super-resolution via deep recursive residual network. In Proceedings of the IEEE Conference on Computer Vision and Pattern Recognition, Honolulu, HI, USA, 21–26 July 2017; pp. 3147–3155.
12. Lim, B.; Son, S.; Kim, H.; Nah, S.; Mu Lee, K. Enhanced deep residual networks for single image super-resolution. In Proceedings of the IEEE Conference on Computer Vision and Pattern Recognition Workshops, Honolulu, HI, USA, 21–26 July 2017; pp. 136–144.
13. Tong, T.; Li, G.; Liu, X.; Gao, Q. Image super-resolution using dense skip connections. In Proceedings of the IEEE International Conference on Computer Vision, Venice, Italy, 22–29 October 2017; pp. 4799–4807.
14. Dudczyk, J.; Rybak, Ł. Application of Data Particle Geometrical Divide Algorithms in the Process of Radar Signal Recognition. *Sensors* **2023**, *23*, 8183. [CrossRef]
15. Rybak, Ł.; Dudczyk, J. Variant of data particle geometrical divide for imbalanced data sets classification by the example of occupancy detection. *Appl. Sci.* **2021**, *11*, 4970. [CrossRef]
16. Zhang, Y.; Tian, Y.; Kong, Y.; Zhong, B.; Fu, Y. Residual dense network for image super-resolution. In Proceedings of the IEEE Conference on Computer Vision and Pattern Recognition, Salt Lake City, UT, USA, 18–23 June 2018; pp. 2472–2481.
17. Zhao, M.; Cheng, C.; Zhang, Z.; Hao, X. Deep convolutional networks super-resolution method for reconstructing high frequency information of the single image. In Proceedings of the 2017 2nd International Conference on Image, Vision and Computing (ICIVC), Chengdu, China, 2–4 June 2017; pp. 531–535.
18. Zhou, F.; Li, X.; Li, Z. High-frequency details enhancing DenseNet for super-resolution. *Neurocomputing* **2018**, *290*, 34–42. [CrossRef]

19. Liu, A.; Liu, Y.; Gu, J.; Qiao, Y.; Dong, C. Blind image super-resolution: A survey and beyond. *IEEE Trans. Pattern Anal. Mach. Intell.* **2022**, *45*, 5461–5480. [CrossRef]
20. Zamfir, E.; Conde, M.V.; Timofte, R. Towards real-time 4k image super-resolution. In Proceedings of the IEEE/CVF Conference on Computer Vision and Pattern Recognition, Vancouver, BC, Canada, 17–24 June 2023; pp. 1522–1532.
21. Chen, J.; Li, B.; Xue, X. Scene text telescope: Text-focused scene image super-resolution. In Proceedings of the IEEE/CVF Conference on Computer Vision and Pattern Recognition, Nashville, TN, USA, 20–25 June 2021; pp. 12026–12035.
22. Yue, Z.; Wang, J.; Loy, C.C. Resshift: Efficient diffusion model for image super-resolution by residual shifting. *Adv. Neural Inf. Process. Syst.* **2024**, *13294–13307*.
23. Zhang, M.; Zhang, C.; Zhang, Q.; Guo, J.; Gao, X.; Zhang, J. Essaformer: Efficient transformer for hyperspectral image super-resolution. In Proceedings of the IEEE/CVF International Conference on Computer Vision, Paris, France, 1–6 October 2023; pp. 23073–23084.
24. Lu, Y.; Wang, Z.; Liu, M.; Wang, H.; Wang, L. Learning spatial-temporal implicit neural representations for event-guided video super-resolution. In Proceedings of the IEEE/CVF Conference on Computer Vision and Pattern Recognition, Vancouver, BC, Canada, 17–24 June 2023; pp. 1557–1567.
25. Turco, A.; Gheysens, O.; Nuyts, J.; Duchenne, J.; Voigt, J.U.; Claus, P.; Vunckx, K. Impact of CT-based attenuation correction on the registration between dual-gated cardiac PET and high-resolution CT. *IEEE Trans. Nucl. Sci.* **2016**, *63*, 180–192. [CrossRef]
26. Tantawy, H.M.; Abdelhafez, Y.G.; Helal, N.L.; Kany, A.I.; Saad, I.E. Effect of correction methods on image resolution of myocardial perfusion imaging using single photon emission computed tomography combined with computed tomography hybrid systems. *J. Phys. Commun.* **2020**, *4*, 015011. [CrossRef]
27. Simonyan, K.; Zisserman, A. Very deep convolutional networks for large-scale image recognition. *arXiv* **2014**, arXiv:1409.1556.
28. He, K.; Zhang, X.; Ren, S.; Sun, J. Deep residual learning for image recognition. In Proceedings of the IEEE Conference on Computer Vision and Pattern Recognition, Las Vegas, NV, USA, 27–30 June 2016; pp. 770–778.
29. Li, Z.; Yang, J.; Liu, Z.; Yang, X.; Jeon, G.; Wu, W. Feedback network for image super-resolution. In Proceedings of the IEEE/CVF Conference on Computer Vision and Pattern Recognition, Long Beach, CA, USA, 15–20 June 2019; pp. 3867–3876.
30. Li, S.; Cai, Q.; Li, H.; Cao, J.; Wang, L.; Li, Z. Frequency separation network for image super-resolution. *IEEE Access* **2020**, *8*, 33768–33777. [CrossRef]
31. Haris, M.; Shakhnarovich, G.; Ukita, N. Deep back-projection networks for super-resolution. In Proceedings of the IEEE Conference on Computer Vision and Pattern Recognition, Salt Lake City, UT, USA, 18–23 June 2018; pp. 1664–1673.
32. Yang, C.; Lu, G. Deeply recursive low-and high-frequency fusing networks for single image super-resolution. *Sensors* **2020**, *20*, 7268. [CrossRef] [PubMed]
33. Chen, L.; Zhang, H.; Xiao, J.; Nie, L.; Shao, J.; Liu, W.; Chua, T.S. Sca-cnn: Spatial and channel-wise attention in convolutional networks for image captioning. In Proceedings of the IEEE Conference on Computer Vision and Pattern Recognition, Honolulu, HI, USA, 21–26 July 2017; pp. 5659–5667.
34. Fu, J.; Liu, J.; Tian, H.; Li, Y.; Bao, Y.; Fang, Z.; Lu, H. Dual attention network for scene segmentation. In Proceedings of the IEEE/CVF Conference on Computer Vision and Pattern Recognition, Long Beach, CA, USA, 15–20 June 2019; pp. 3146–3154.
35. Zhang, X.; Wang, T.; Qi, J.; Lu, H.; Wang, G. Progressive attention guided recurrent network for salient object detection. In Proceedings of the IEEE Conference on Computer Vision and Pattern Recognition, Salt Lake City, UT, USA, 18–23 June 2018; pp. 714–722.
36. Liu, Y.; Wang, Y.; Li, N.; Cheng, X.; Zhang, Y.; Huang, Y.; Lu, G. An attention-based approach for single image super resolution. In Proceedings of the 2018 24th International Conference on Pattern Recognition (ICPR), Beijing, China, 20–24 August 2018; pp. 2777–2784.
37. Zhang, Y.; Li, K.; Li, K.; Wang, L.; Zhong, B.; Fu, Y. Image super-resolution using very deep residual channel attention networks. In Proceedings of the European Conference on Computer Vision (ECCV), Munich, Germany, 8–14 September 2018; pp. 286–301.
38. Lu, Y.; Zhou, Y.; Jiang, Z.; Guo, X.; Yang, Z. Channel attention and multi-level features fusion for single image super-resolution. In Proceedings of the 2018 IEEE Visual Communications and Image Processing (VCIP), Taichung, Taiwan, 9–12 December 2018; pp. 1–4.
39. Hu, Y.; Li, J.; Huang, Y.; Gao, X. Channel-wise and spatial feature modulation network for single image super-resolution. *IEEE Trans. Circuits Syst. Video Technol.* **2019**, *30*, 3911–3927. [CrossRef]
40. Timofte, R.; Agustsson, E.; Van Gool, L.; Yang, M.H.; Zhang, L. Ntire 2017 challenge on single image super-resolution: Methods and results. In Proceedings of the IEEE Conference on Computer Vision and Pattern Recognition Workshops, Honolulu, HI, USA, 21–26 July 2017; pp. 114–125.
41. Bevilacqua, M.; Roumy, A.; Guillemot, C.; Alberi-Morel, M.L. *Low-Complexity Single-Image Super-Resolution Based on Nonnegative Neighbor Embedding*; BMVA Press: Durham, UK, 2012.
42. Zeyde, R.; Elad, M.; Protter, M. On single image scale-up using sparse-representations. In Proceedings of the Curves and Surfaces: 7th International Conference, Avignon, France, 24–30 June 2010; Revised Selected Papers 7; Springer: Berlin/Heidelberg, Germany, 2012; pp. 711–730.
43. Arbelaez, P.; Maire, M.; Fowlkes, C.; Malik, J. Contour detection and hierarchical image segmentation. *IEEE Trans. Pattern Anal. Mach. Intell.* **2010**, *33*, 898–916. [CrossRef] [PubMed]

44. Huang, J.B.; Singh, A.; Ahuja, N. Single image super-resolution from transformed self-exemplars. In Proceedings of the IEEE Conference on Computer Vision and Pattern Recognition, Boston, MA, USA, 7–12 June 2015; pp. 5197–5206.
45. Matsui, Y.; Ito, K.; Aramaki, Y.; Fujimoto, A.; Ogawa, T.; Yamasaki, T.; Aizawa, K. Sketch-based manga retrieval using manga109 dataset. *Multimed. Tools Appl.* **2017**, *76*, 21811–21838. [CrossRef]
46. Wang, Z.; Bovik, A.C.; Sheikh, H.R.; Simoncelli, E.P. Image quality assessment: From error visibility to structural similarity. *IEEE Trans. Image Process.* **2004**, *13*, 600–612. [CrossRef] [PubMed]
47. Wang, L.; Wang, Y.; Liang, Z.; Lin, Z.; Yang, J.; An, W.; Guo, Y. Learning parallax attention for stereo image super-resolution. In Proceedings of the IEEE/CVF Conference on Computer Vision and Pattern Recognition, Long Beach, CA, USA, 15–20 June 2019; pp. 12250–12259.
48. Jiang, K.; Wang, Z.; Yi, P.; Jiang, J. Hierarchical dense recursive network for image super-resolution. *Pattern Recognit.* **2020**, *107*, 107475. [CrossRef]
49. Ahn, N.; Kang, B.; Sohn, K.A. Fast, accurate, and lightweight super-resolution with cascading residual network. In Proceedings of the European Conference on Computer Vision (ECCV), Munich, Germany, 8–14 September 2018; pp. 252–268.
50. Hui, Z.; Gao, X.; Yang, Y.; Wang, X. Lightweight image super-resolution with information multi-distillation network. In Proceedings of the 27th ACM International Conference on Multimedia, Nice, France, 21–25 October 2019; pp. 2024–2032.
51. Li, W.; Zhou, K.; Qi, L.; Jiang, N.; Lu, J.; Jia, J. Lapar: Linearly-assembled pixel-adaptive regression network for single image super-resolution and beyond. *Adv. Neural Inf. Process. Syst.* **2020**, *33*, 20343–20355.
52. Zhang, K.; Zuo, W.; Zhang, L. Learning a single convolutional super-resolution network for multiple degradations. In Proceedings of the IEEE Conference on Computer Vision and Pattern Recognition, Salt Lake City, UT, USA, 18–23 June 2018; pp. 3262–3271.
53. Wang, X.; Wang, Q.; Zhao, Y.; Yan, J.; Fan, L.; Chen, L. Lightweight single-image super-resolution network with attentive auxiliary feature learning. In Proceedings of the Asian Conference on Computer Vision, Kyoto, Japan, 30 November–4 December 2020.
54. Behjati, P.; Rodriguez, P.; Tena, C.F.; Mehri, A.; Roca, F.X.; Ozawa, S.; Gonzalez, J. Frequency-based enhancement network for efficient super-resolution. *IEEE Access* **2022**, *10*, 57383–57397. [CrossRef]
55. Cai, J.; Zeng, H.; Yong, H.; Cao, Z.; Zhang, L. Toward real-world single image super-resolution: A new benchmark and a new model. In Proceedings of the IEEE/CVF International Conference on Computer Vision, Seoul, Republic of Korea, 27 October–2 November 2019; pp. 3086–3095.
56. Wei, P.; Xie, Z.; Lu, H.; Zhan, Z.; Ye, Q.; Zuo, W.; Lin, L. Component divide-and-conquer for real-world image super-resolution. In Proceedings of the Computer Vision–ECCV 2020: 16th European Conference, Glasgow, UK, 23–28 August 2020; Proceedings, Part VIII 16; Springer: Berlin/Heidelberg, Germany, 2020; pp. 101–117.